

Large Hyperfine Coupling Arising from Pseudo- 2S Ground States in a Series of Lutetium(II) Metallocene Complexes

Danh X. Ngo,[○] K. Randall McClain,^{*,○} Jakub Hrubý, Yannick J. Franzke, Krishnendu Kundu, Hyunchul Kwon, Colin A. Gould, Benjamin G. Harvey, Stephen Hill,^{*} and Jeffrey R. Long^{*}



Cite This: *J. Am. Chem. Soc.* 2025, 147, 13799–13807



Read Online

ACCESS |



Metrics & More

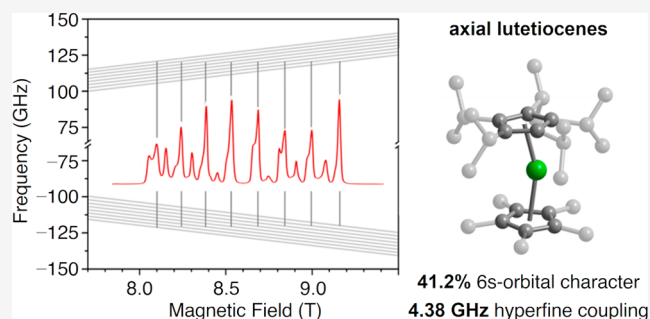


Article Recommendations



Supporting Information

ABSTRACT: The synthesis of molecules with strong coupling between electronic and nuclear spins represents an important challenge in molecular quantum information science. Here, we report the synthesis and characterization of the divalent lutetium metallocene complexes $\text{Lu}(\text{Cp}^{\text{Me}_5})(\text{Cp}^{\text{iPr}_3})$ (Cp^{Me_5} = pentamethylcyclopentadienyl; Cp^{iPr_3} = pentaisopropylcyclopentadienyl), $\text{Lu}(\text{Cp}^{\text{iPr}_4\text{Et}})_2$ ($\text{Cp}^{\text{iPr}_4\text{Et}}$ = ethyltetraisopropylcyclopentadienyl), and $\text{Lu}(\text{Cp}^{\text{iPr}_4})_2$ (Cp^{iPr_4} = tetraisopropylcyclopentadienyl). The molecular structures of these complexes, as determined through single-crystal X-ray diffraction, feature a common bent sandwich geometry, with average Cp–Lu–Cp angles ranging from 159.9° to 152.6°. Analysis of continuous-wave electron paramagnetic resonance (EPR) spectra for the complexes reveals nearly isotropic g tensors with only a slight deviation from that of a free electron. Moreover, an extremely large splitting of the eight-line spectra indicates the presence of strong hyperfine coupling, and simulations provide isotropic hyperfine coupling constants of $A_{\text{iso}} = 4.38, 4.30,$ and 4.17 GHz across the series, where the value of A_{iso} is found to decrease as the Cp–Lu–Cp angle becomes more acute. Notably, these values are the largest yet observed for any lanthanide complex. Moreover, EPR and computational analysis show that the large values of A_{iso} stem from large s -orbital character—up to 41.2%—in the corresponding singly occupied molecular orbitals. To our knowledge, this degree of s -character in a molecular orbital is the largest yet reported for an open-shell isolable complex. These results outline a general strategy toward the isolation of paramagnetic molecules with strong hyperfine coupling and highly isotropic doublet electronic ground states.



INTRODUCTION

The presence of strong hyperfine coupling between nuclear and electronic spins in certain materials gives rise to exotic physics that underlies numerous applications in quantum information science, namely, the design of quantum bits—or qubits—which host highly coherent superpositions of quantum states that can be initialized, manipulated, and detected. For instance, the hyperfine transitions of ^{117}Sn vacancy centers in diamond can be optically addressed to effect initialization and readout of a nuclear spin owing to the large magnitude of the hyperfine coupling to the ^{117}Sn nucleus, which greatly exceeds the natural optical linewidth of the system.¹ Additionally, hyperfine coupling forms the basis of atomic clock physics, and the use of spin clock transitions has been well studied in defect states of various solid-state materials.^{2–8} In particular, bismuth defects in silicon possess an electronic structure with spin sublevels that are first-order insensitive to the applied magnetic field, forming the basis of a clock qubit.² Considerable computational and experimental effort has been directed toward discovering other spin defects with such properties.⁹ Beyond enabling optical initialization and readout as well as extending coherence times in qubits, large values of the

hyperfine constant A energetically resolve nuclear spin sublevels in Tb^{3+} single-molecule magnets, enabling electrically driven coherent control of nuclear spin states via the hyperfine Stark effect.¹⁰ Therefore, strong hyperfine interactions can facilitate various desirable functions within quantum information applications.

Despite considerable advances and applications in spin-defect quantum technology, solid-state-based quantum devices face several intrinsic limitations, such as the lack of atomic precision in the placement of individual quantum centers, the inability to scale these systems in a predictive manner, and the challenges of materials discovery. Alternatively, extending these phenomena to molecular systems offers an intriguing approach, as the composition and geometry of molecules can be programmed and tuned at the atomic level through simple

Received: January 31, 2025

Revised: March 8, 2025

Accepted: March 12, 2025

Published: April 9, 2025



coordination chemistry, and such compounds can be obtained in single-crystalline form.¹¹

Recent work has demonstrated that lanthanide complexes, including Lu^{2+} complexes with large hyperfine constants, can be employed as clock qubits with long coherence times.^{12–14} In conventional Zeeman-based spin qubits, minute changes in the local magnetic field lead to significant shifts in the frequency of the transition, thus promoting decoherence (Figure 1a). In contrast, for a hyperfine coupling-based clock

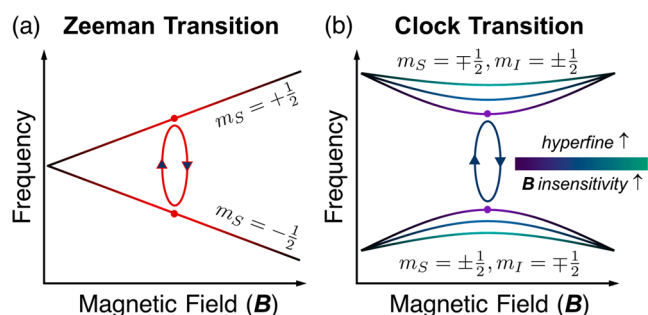


Figure 1. Cartoon depiction of spin transitions in Zeeman (a) and clock (b) qubits. The first-order field insensitivity of a clock qubit renders its transition frequency insensitive to fluctuations in the magnetic field (represented by a flatter frequency–magnetic field profile), thus engendering longer coherence times. Increasing the frequency of the clock transition Δ also increases the second-order field insensitivity of the clock transition and thus extends the flat region across a greater range of magnetic field.

qubit, avoided energy crossings appear in the Zeeman splitting of qubit basis states as a result of strong hyperfine coupling of nuclear and electronic spins. At the avoided crossing, the frequency (f) of the electron paramagnetic resonance (EPR) is first-order insensitive to local magnetic induction (B) and consequently to magnetic field fluctuations, thereby extending the coherence time (Figure 1b).

Molecular clock qubits^{13–20} offer the tunability required to iteratively design species with spin clock transitions that are more impervious to decoherence, namely, by targeting the second-order insensitivity to the local magnetic induction, as described by the equation $d^2f/dB^2 = \gamma_e^2/\Delta$, where γ_e is the electron gyromagnetic ratio and Δ is the frequency of the spin clock transition.^{17,19} As the frequency of the clock transition Δ increases, the clock transition incurs greater second-order insensitivity to magnetic field fluctuations and consequently prolonged coherence.^{19,20} As such, the synthesis of molecular complexes with spin clock transitions characterized by systematically increasing Δ can pave the way toward clock qubits with long coherence times, especially once Δ approaches commercial pulsed EPR spectrometer frequencies beyond the X-band such as the Q-band (34 GHz).

One synthetic strategy to isolate molecules with strong hyperfine coupling is through targeting species with singly occupied molecular orbitals (SOMOs) of high s-orbital parentage.^{21–23} Since s orbitals feature nonzero electron density at the nucleus, such complexes can exhibit significant interaction between electronic and nuclear spins, corresponding to large values of the hyperfine constant. Nevertheless, for the vast majority of paramagnetic molecules, little s-orbital character of the ground state is observed—across a range of molecular archetypes, including main group radicals and transition metal coordination complexes—owing to the

presence of SOMOs of primarily p-, d-, or f-orbital character. Such small degrees of s-orbital character are manifested as only modest values of the hyperfine coupling constant. Indeed, chemical species with rigorous ^2S ground states arising from spherical symmetry are limited to gas-phase ions and atoms, with several of these species constituting state-of-the-art technologies in the field of quantum information science.^{24–26}

In exceptional cases, certain molecules have been reported with point group symmetries that permit greater s-orbital admixture from an excited state to the ground state. Among these rare examples are the anionic trigonal Lu^{2+} complexes $[\text{Lu}(\text{Cp}^{\text{SiMe}_3})_3]^-$ ($\text{Cp}^{\text{SiMe}_3} = \text{C}_5\text{H}_4\text{SiMe}_3$), $[\text{Lu}(\text{NR}_2)_3]^-$ ($\text{NR}_2 = \text{N}(\text{SiMe}_3)_2$), $[\text{Lu}(\text{OAr})_3]^-$ ($\text{OAr} = 2,6\text{-Ad}_2\text{-4-}^t\text{Bu-C}_6\text{H}_2\text{O}$, where Ad is adamantyl) with GHz-scale hyperfine constants determined by EPR spectroscopy corresponding to SOMOs with s-orbital parentages of 10%, 23%, and 33%, respectively.^{14,27} The presence of such large s-orbital character in the electronic ground states of these molecules can be understood through a qualitative orbital energy correlation diagram (Figure 2). First, consider the electronic structure of a free

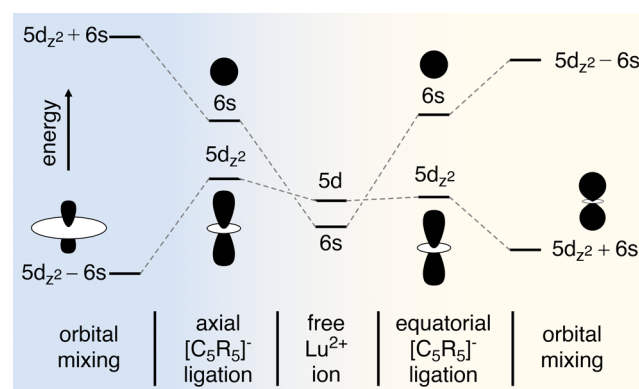


Figure 2. Qualitative energy correlation diagram for the $6s$ and $5d_{z^2}$ orbitals of a Lu^{2+} ion upon ligation of cyclopentadienyl ligands $[\text{C}_5\text{R}_5]^-$ in an equatorial arrangement versus an axial arrangement, prior to and after symmetry-allowed orbital mixing considerations. Metal-based orbitals are of a totally symmetric irreducible representation. Ligation considers interaction with ligand-based symmetry-adapted linear combinations of atomic orbitals, which transform under the totally symmetric irreducible representation. The closer $6s$ and $5d_{z^2}$ orbital energies in the case of axial cyclopentadienyl ligation gives rise to enhanced s-orbital character in the singly occupied molecular orbitals of the corresponding axial Lu^{2+} metallocene molecules.

Lu^{2+} ion, where the $6s$ orbital is slightly lower in energy than the $5d_{z^2}$ orbital.²⁸ Upon equatorial cyclopentadienyl ligation, the $6s$ orbital undergoes a larger energetic destabilization than does the $5d_{z^2}$ orbital, situating the $6s$ orbital higher in energy than the $5d_{z^2}$ orbital. Finally, symmetry-allowed mixing between these orbitals in the totally symmetric irreducible representation gives rise to a $5d_{z^2} + 6s$ hybrid orbital that is lower in energy and a $5d_{z^2} - 6s$ hybrid orbital that is higher in energy, with the degree of mixing determined by the energy gap between the $6s$ and $5d_{z^2}$ orbitals.

Inspection across the series of previously reported trigonal Lu^{2+} complexes reveals a gradual structural distortion from a trigonal planar to a trigonal pyramidal coordination geometry, which accompanies an increase in $6s$ -orbital parentage. This trend likely reflects a greater relative crystal-field-induced destabilization of the $5d_{z^2}$ orbital compared to the $6s$ orbital

upon distortion to a trigonal pyramidal geometry; the consequently smaller energetic gap between the two orbitals results in greater $6s-5d_z^2$ mixing (Figure 2). Following this logic, we hypothesized that a more pronounced structural distortion toward an axial bis-cyclopentadienyl geometry would induce an even greater relative energetic destabilization of the $5d_z^2$ orbital compared to the $6s$ orbital (Figure 2), allowing these two orbitals to mix more extensively and give rise to higher degrees of ground state s -orbital character. Indeed, previous work has shown that encapsulating divalent ions such as Y^{2+} ($A = 500$ MHz, 40% s -orbital character),²⁹ La^{2+} (2 GHz, 33%),²⁹ and Tl^{2+} (35 GHz, 17%)^{30,31} in axial coordination environments can give rise to significant s -orbital character in the ground state. Moreover, density functional theory calculations have suggested the presence of considerable s -orbital character in axial lanthanide metallocene, or $Ln(C_5R_5)_2$, complexes.²⁹

Herein, we report the synthesis and crystal structures of three Lu^{2+} metallocene complexes, with EPR spectroscopy and computational analysis showing significant hyperfine coupling stemming from the nearly maximal s -orbital character of the doublet ground state. Moreover, within the series of three Lu^{2+} metallocene molecules, the hyperfine coupling and $6s$ orbital character are found to systematically increase as the $Cp-Lu-Cp$ angle approaches linearity.

RESULTS AND DISCUSSION

Synthesis and Structural Characterization. The axial Lu^{2+} metallocene complexes $Lu(Cp^{Me_5})(Cp^{iPr_5})$ (**1**), $Lu(Cp^{iPr_4Et})_2$ (**2**), and $Lu(Cp^{iPr_4})_2$ (**3**) (Figure 3) were

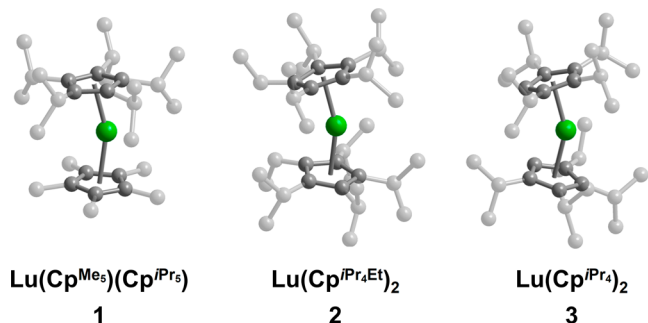


Figure 3. Molecular structures of complexes **1–3** from single-crystal X-ray diffraction. Green and gray spheres represent Lu and C atoms, respectively. In the case of **1**, the structure shown corresponds to the structural isomer with 87% abundance. Hydrogen atoms have been omitted for clarity. Only one of the two molecules in the unit cell of **3** is shown for clarity.

synthesized via salt metathesis followed by chemical reduction using methods based on the previously published lanthanocenes, $Ln(Cp^{iPr_5})_2$.^{29,32} For heteroleptic **1**, the trivalent dimer, $(Cp^{iPr_5})_2Lu_2I_4$, which was synthesized from LuI_3 and $NaCp^{iPr_5}$ in a manner similar to the previously published $(Cp^{iPr_5})_2Ln_2I_4$ compounds,³³ was subjected to salt metathesis with $NaCp^{Me_5}$ in toluene at high temperature to yield the putative compound $Lu(Cp^{Me_5})(Cp^{iPr_5})I$. The crude intermediate was dissolved in benzene and reduced to the divalent Lu^{2+} metallocene by stirring with excess KC_8 over several days at room temperature. Following solvent removal and crystallization from hexane, pure $Lu(Cp^{Me_5})(Cp^{iPr_5})$ was isolated as yellow plate-shaped

crystals whose electronic absorption spectra and infrared spectra are documented in Figures S5 and S14–S16.

In the case of **2** and **3**, salt metathesis between LuI_3 and the corresponding sodium cyclopentadienide salts in toluene solvent at high temperature led to the putative iodide intermediates $Lu(Cp^{iPr_4Et})_2I$ and $Lu(Cp^{iPr_4})_2I$. The crude residues were dissolved in benzene and converted to the desired Lu^{2+} metallocenes by stirring with excess KC_8 at room temperature for several days. Following solvent removal and crystallization from hexane or pentane, analytically pure **2** and **3** were isolated as dark yellow prismatic crystals whose electronic absorption spectra and infrared spectra are documented in Figures S6, S7, and S17–S22. Both solid-state samples and alkane solutions of the Lu^{2+} metallocenes were found to be stable at room temperature over many months under argon and can be recrystallized from boiling hexane without noticeable decomposition but decay rapidly in the presence of air and moisture.

The solid-state structures of **1**, **2**, and **3** were determined by single-crystal X-ray diffraction analyses (Tables 1, S2–S4, S6–S8, Figures S9–S11). All exhibit a bent geometry with average $Cp-Lu-Cp$ angles ranging from $152.57(7)^\circ$ to $159.91(9)^\circ$.

In heteroleptic complex **1**, the lutetium atom is disordered over two positions in an 87:13 ratio. Such positional disorder of the central lanthanide ion is commonly observed in bent lanthanide metallocenes.^{34,35} This positional disorder yields two sets of $Cp-Lu-Cp$ angles and $[Lu-Cp^{Me_5}, Lu-Cp^{iPr_5}]$

Table 1. Summary of Parameters Obtained from X-ray Diffraction and EPR Analysis^a

	1	2	3
$\angle Cp-Lu-Cp$ (deg)	158.8(7) ^a 161.0(5) ^b	156.96(17)	152.68(10) ^c 152.46(11) ^f
$Cp-Lu$ (Å)	2.253(2) ^{a,c} 2.314(2) ^{a,d} 2.206(7) ^{b,c} 2.345(8) ^{b,d}	2.315(3)	2.296(3) ^e 2.306(3) ^e 2.295(3) ^f 2.311(3) ^f
$\angle Cp-Lu-Cp_{mean}$ (deg)	159.91(9)	156.96(17)	152.57(7)
$Cp-Lu_{mean}$ (Å)	2.282(1)	2.315(3)	2.302(2)
g_x	1.982	1.986	1.985
g_y	1.982	1.986	1.985
g_z	1.995	1.996	1.990
$ g_x - g_e $	0.019	0.016	0.017
$ g_y - g_e $	0.019	0.016	0.017
$ g_z - g_e $	0.007	0.006	0.012
$g_{iso,exp}$	1.987	1.989	1.987
$g_{iso,calc}$	1.989	1.992	1.991
A_x (GHz)	4.35	4.25	4.10
A_y (GHz)	4.35	4.25	4.10
A_z (GHz)	4.43	4.40	4.30
$A_{iso,exp}$ (GHz)	4.38	4.30	4.17
$A_{iso,calc}$ (GHz)	4.34	4.28	4.18
Q_x (MHz) ^g	70	100	60
SOMO $6s$ orbital character	41.2%	40.5%	39.2%

^aIn **1**, angles and distances correspond to two structurally disordered components with occupancies of ^a87% and ^b13% as derived from single-crystal X-ray diffraction analysis. Additionally, in heteroleptic **1**, distances correspond to the ^c Cp^{Me_5} and ^d Cp^{iPr_5} ligands. In **3**, angles and distances correspond to those of two^{e,f} crystallographically inequivalent molecules of **3** in the asymmetric unit of the crystal structure. ^g $Q_x - Q_y = 0$ for **1–3**.

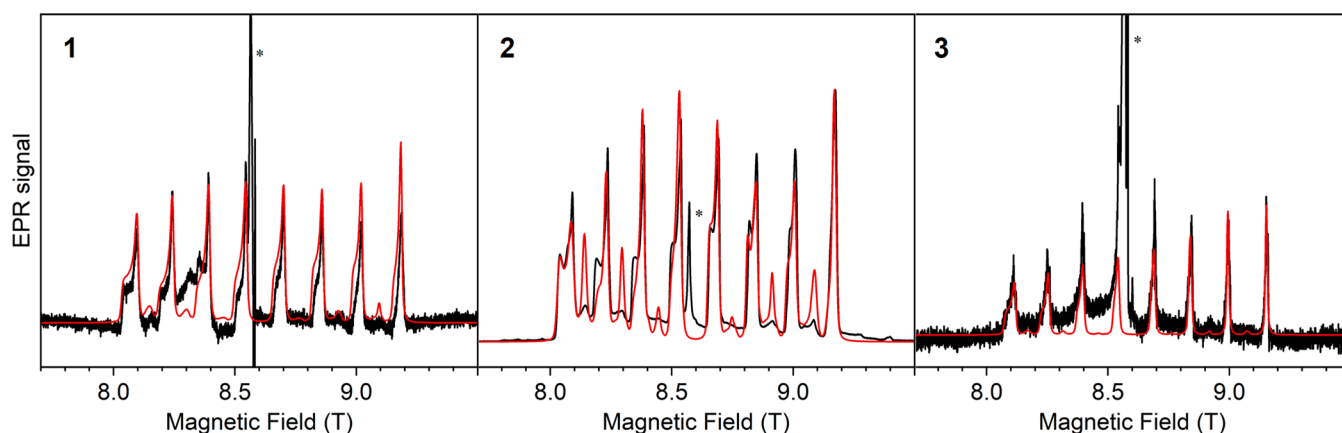


Figure 4. High-field, high-frequency (240 GHz) continuous-wave electron paramagnetic resonance spectra of 1–3 measured at 5 K. Experimental data and corresponding simulations are colored black and red, respectively. Asterisks designate peaks associated with an unidentified $g = 2$ impurity.

distance pairs. The 87%-occupancy disorder component—determined by allowing the lutetium occupancy to freely refine—exhibits a Cp–Lu–Cp angle of $158.8(7)^\circ$, a Lu–Cp^{Me_s} distance of 2.253(2) Å, and a Lu–Cp^{iPr_s} distance of 2.314(2) Å. Meanwhile, the 13%-occupancy disorder component exhibits a Cp–Lu–Cp angle of $161.0(5)^\circ$, a Lu–Cp^{Me_s} distance of 2.206(7) Å, and a Lu–Cp^{iPr_s} distance of 2.345(8) Å. In total, **1** exhibits a weighted average Cp–Lu–Cp angle of $159.91(9)^\circ$ and a weighted average Cp–Lu distance of 2.282(1) Å.

In **2**, asymmetry in the steric profile of the [Cp^{iPr_sEt}][−] ligand leads to a more acute Cp–Lu–Cp angle, as the steric clash between opposite [Cp^{iPr_sEt}][−] ligands is mitigated at the ethyl substituent compared to the more sterically encumbered isopropyl substituents. Homoleptic compound **2** exhibits a Cp–Lu–Cp angle of $156.96(17)^\circ$ and a Cp–Lu distance of 2.315(3) Å. The more acute average Cp–Lu–Cp angle and longer average Cp–Lu distances indicate a less axial crystal field in **2** compared to **1**.

In the crystal structure of **3**, two crystallographically nonequivalent molecules exhibit Cp–Lu–Cp angles of $152.46(11)^\circ$ and $152.68(10)^\circ$, each containing short Cp–Lu distances of 2.295(3) and 2.296(3) Å, respectively, and long Cp–Lu distances of 2.311(3) and 2.308(3) Å, respectively, resulting in an average Cp–Lu–Cp angle of $152.57(7)^\circ$ and an average Cp–Lu distance of 2.302(2) Å. Particularly low steric encumbrance at the unsubstituted position of the [Cp^{iPr_s}][−] ring in **3** leads to the most acute Cp–Lu–Cp angle among 1–3, and thus **3** features the least axial crystal field among the three Lu²⁺ metallocene complexes.

Electron Paramagnetic Resonance Spectroscopy. To probe the extent of hyperfine coupling in 1–3, continuous-wave electron paramagnetic resonance (CW-EPR) spectra were collected on ground microcrystalline powders of 1–3 at $T = 5$ K, at frequencies up to 384 GHz and magnetic fields of up to 15 T (see Supporting Information for experimental details; additional variable-field CW-EPR spectra are included in Figures S23–S25). CW-EPR spectra, collected at $f = 240$ GHz and $T = 5$ K, at magnetic fields of up to 10 T, for 1–3 (Figure 4) all exhibit an eight-line pattern characteristic of an $S = 1/2$ state split via the interaction with an $I = 7/2$ ¹⁷⁵Lu nucleus (97.41% natural abundance). Simulations of the spectra reveal the presence of nearly isotropic g tensors for 1–3, with all g -

tensor components g_x , g_y , and g_z deviating less than 0.02 from the free electron value of 2.0023. Importantly, the isotropic nature of these g values is in contrast to those previously reported for divalent lutetium molecules with trigonal crystal fields,^{14,27} consistent with the presence of higher s -orbital character in the SOMOs of these axial Lu²⁺ metallocene complexes.

Explicitly, the degree of deviation from the free electron value of $g_e = 2.0023$ for the g tensor of a spin due to second-order orbital angular momentum can be described by the following proportionality expression:

$$|g - g_e| \propto \lambda \cdot \langle j|\hat{H}l_i\rangle / \Delta_{ij} \quad (1)$$

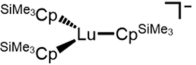
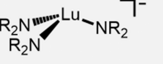
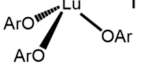
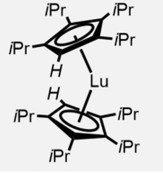
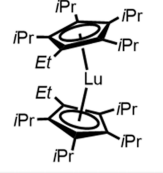
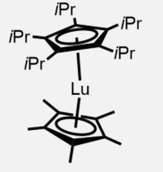
where λ is the spin–orbit coupling constant, $\langle j|\hat{H}l_i\rangle$ is the matrix element corresponding to spin–orbit coupling-induced mixing of ground (i) and excited (j) state orbitals, and Δ_{ij} is the energy gap between states i and j .³⁶ In the case of 1–3, a large value of λ arises owing to the large atomic number of Lu. As such, the observed isotropy of the unpaired spin in these complexes instead likely stems from a combination of insignificant spin–orbit coupling-induced mixing of the electronic states and a substantial energy gap Δ_{ij} . Indeed, $\langle j|\hat{H}l_i\rangle$ is expected to be minimal for orbitals with significant s character due to the spherical symmetry of the s orbital. Moreover, the energy gap Δ_{ij} should increase with the degree of $6s$ orbital mixing and consequently stabilize the $6s-5d_{z^2}$ hybrid orbital, thereby energetically isolating it from higher-energy $5d$ orbitals. These results suggest that the isotropy observed for the unpaired spin in 1–3 stems from a SOMO with a significant degree of s -orbital character.

The hyperfine coupling constant, A , which provides a quantitative measure of the strength of interaction between electronic and nuclear spins, is directly correlated to the degree of s -orbital character of the electronically populated orbital, since the nonzero electron density at the nucleus of an s orbital gives rise to significant electronic–nuclear coupling. To extract the hyperfine coupling constants associated with 1–3, simulations of the EPR spectra at 5 K were performed according to the Hamiltonian in eq 2 using EasySpin.³⁷

$$\hat{H} = \mu_B \vec{B} \cdot \vec{g}_e \cdot \hat{S} - \mu_N g_N \vec{B} \cdot \hat{I} + \hat{S} \cdot \vec{A} \cdot \hat{I} + \hat{I} \cdot \vec{Q} \cdot \hat{I} \quad (2)$$

where μ_B is the Bohr magneton, μ_N is the nuclear magneton, \vec{B} is the applied magnetic field, \vec{g}_e is the g -tensor of the electron,

Table 2. Comparison of EPR Parameters for Lu²⁺ Complexes with Strong Hyperfine Coupling^{abc}

	g_x, g_y, g_z	g_{iso}	$g_e - g_{\text{iso}}$	A_{iso} (GHz)	SOMO 6s character	ref.
	1.966, 1.966, 1.998	1.977	0.025	1.1	10%	27 ^a
	1.882, 1.898, 2.000	1.927	0.075	2.4	23%	14 ^b
	1.915, 1.915, 2.000	1.943	0.059	3.5	33%	14 ^c
	1.985, 1.985, 1.990	1.987	0.015	4.17	39.2%	this work
	1.986, 1.986, 1.996	1.989	0.013	4.30	40.5%	this work
	1.982, 1.982, 1.995	1.987	0.015	4.38	41.2%	this work

^a(Cp^{SiMe3})⁻ = C₅H₄SiMe₃⁻. ^bNR₂⁻ = N(SiMe₃)₂⁻. ^cOAr⁻ = 2,6-Ad₂-4^tBu-C₆H₂O⁻.

g_N is the g -factor for the nucleus, \hat{S} is the electron spin operator, \hat{I} is the nuclear spin operator, \vec{A} is the hyperfine coupling tensor, and \vec{Q} is a matrix that represents the nuclear quadrupole interaction tensor.

The eight lines present in each EPR spectrum correspond to eight allowed transitions from the $M_S = -1/2$ to the $M_S = +1/2$ manifold (Figure 4). In line with the observed g tensor isotropy and minimal deviations from $g_e = 2.0023$, these simulations reveal the presence of immense hyperfine coupling across the series of Lu²⁺ metallocenes, with isotropic coupling constants of $A_{\text{iso}} = 4.38 \pm 0.05$ GHz, 4.30 ± 0.05 GHz, and 4.17 ± 0.05 GHz, respectively, for 1, 2, and 3 (Table 1). The hyperfine tensors $A = [4.35, 4.35, 4.43]$ GHz, $A = [4.25, 4.25, 4.40]$ GHz, and $A = [4.10, 4.10, 4.30]$ GHz, for 1, 2, and 3, respectively, display little anisotropy, once again highlighting the isotropic nature of the doublet ground states in 1–3 (Table 1). The peak structure of these eight allowed transitions is governed by slight g and A anisotropy, as well as quadrupolar splitting whose magnitude is comparable to that of previously reported [Lu(OAr)₃]⁻; beyond this eight-line pattern, additional peaks indicative of hyperfine coupling to the $I = 7$ ¹⁷⁶Lu nucleus (2.59% natural abundance) are observed (Figures S24 and S26, Tables 1 and S9).¹⁴

To our knowledge, the value of the hyperfine coupling constant obtained for 1 is the largest yet observed for any lanthanide complex, eclipsing cubic Pr^{IV} sites in Pr:BaSnO₃ ($A_{\text{iso}} = 1.8$ GHz),³⁸ the axial lanthanocene complex La(Cp^{iPr})₂

($A_{\text{iso}} = 2$ GHz),²⁹ and most notably the trigonal pyramidal complex [Lu(OAr)₃]⁻ ($A_{\text{iso}} = 3.5$ GHz),¹⁴ exceeding the previous lanthanide record by nearly 25% (see Table 2). This value of 4.38 GHz also eclipses the previous non-Tl record holder, a Bi^{II} complex Bi^{II}((ArN)[Si]O[Si](NAr)) (Ar = 2,6-diisopropylphenyl, [Si] = SiMe₂) with $A = [-2.804, -3.930, -4.764]$ GHz ($|A_{\text{iso}}| = 3.833$ GHz) and $g = [1.621, 1.676, 1.832]$ ($g_{\text{iso}} = 1.710$).³⁹ Not only do 1–3 exhibit larger A_{iso} and more isotropic A tensors than this Bi^{II} complex, 1–3 also have more isotropic g tensors and an s -orbital character at least eight times that of the 5% in the Bi^{II} complex. Similar to Bi, which boasts $A_{\text{iso,max}} = 77.53$ GHz for theoretical 100% s -orbital character,⁴⁰ Tl possesses inherently a large Fermi contact interaction with $A_{\text{iso,max}} = 183.80$ GHz,⁴⁰ giving rise to large hyperfine coupling constants. Indeed, the largest hyperfine coupling constant observed in a molecule belongs to a linear, two-coordinate Tl^{II} anion (NBu₄)[Tl^{II}(Pt(C₆F₅)₄)₂]³¹ with $A = [35.88, 35.88, 33.97]$ GHz ($A_{\text{iso}} = 34.61$ GHz) and $g = [1.924, 1.924, 2.489]$ ($g_{\text{iso}} = 2.113$), but the s -orbital character (17%) is less than half of that of 1–3. Additionally, the g tensors of this Tl^{II} complex are more anisotropic than those of 1–3. While the more anisotropic g tensors are partly due to the increased atomic number of Tl relative to Lu, we postulate that these differences in the EPR parameters arise mainly from the lower s -orbital character in (NBu₄)[Tl^{II}(Pt(C₆F₅)₄)₂] compared to that of 1–3, the discussion of which follows.

The degree of s -orbital character in a spin-bearing molecular orbital can be estimated by examining how the experimentally

determined hyperfine constant compares to a theoretical maximum hyperfine constant for an ns orbital with single occupation.⁴⁰ For instance, considering the theoretical maximum of $A_{\text{iso,max}} = 10.63$ GHz for the Lu nucleus and the experimental value of $A_{\text{iso}} = 4.38$ GHz for **1**, the s -orbital character can be estimated as $4.38 \text{ GHz}/10.63 \text{ GHz} = 41.2\%$. This exceeds the previous highest percentage of s -orbital character observed in a molecule, 40%, as observed in $\text{Y}(\text{Cp}^{\text{iPr}_5})_2$.²⁹ **1** also exhibits an A_{iso} nearly an order of magnitude larger than the 505 MHz observed for $\text{Y}(\text{Cp}^{\text{iPr}_5})_2$. Notably, the A_{iso} values of **1–3** vastly exceed their early lanthanide counterpart $\text{La}(\text{Cp}^{\text{iPr}_5})_2$ ($A_{\text{iso}} = 2$ GHz, s -orbital character = 33%) likely due to the relativistic contraction of the $6s$ orbitals and relativistic expansion of the $5d$ orbitals moving from the early lanthanides to the late lanthanides; the resultant enhanced energetic proximity of the $6s$ and $5d$ orbitals for Lu corresponds to greater s -orbital character in **1–3** compared to $\text{La}(\text{Cp}^{\text{iPr}_5})_2$. This is also reflected in more isotropic g tensors in **1–3** compared to $\text{La}(\text{Cp}^{\text{iPr}_5})_2$ ($g_x = g_y = 1.92$, $g_z = 1.595$).²⁹ In summary, these results demonstrate a synthetic approach to isolating molecules with ground states approaching the ^2S limit.

While these results show that moving from trigonal to axial geometries engenders an increase in the hyperfine coupling constant via an increase in the s -orbital character of the SOMO, further manipulation of the degree of axiality within a series of axial Lu^{2+} metallocenes can allow for fine-tuning of the s -orbital character. Compound **3**, which exhibits the most acute Cp–Lu–Cp angle and thus the least axial crystal field, is associated with the lowest isotropic hyperfine coupling constant of $A_{\text{iso}} = 4.17$ GHz. A less acute Cp–Lu–Cp angle in **2** results in a larger $A_{\text{iso}} = 4.30$ GHz. Compound **1** exhibits the most axial Cp–Lu–Cp coordination geometry among **1–3**; the greater degree of $5d_z^2$ orbital destabilization results in the largest A_{iso} value among **1–3** of 4.38 GHz.

Although we observed two different Lu environments in **1** and **3** from the analysis of X-ray diffraction data in these compounds, each EPR spectrum was best modeled with one set of g and hyperfine tensors. Indeed, using a two-site model to simulate the EPR data did not yield more reasonable simulations than those obtained by the one-site model discussed here. This result indicates that the disordered components in the crystal structure of **1** display one effective structure within EPR line width considerations, and the same is likely true for the two distinct molecules in the crystal structure of **3**.

Computational Analysis. Density functional theory (DFT) calculations were carried out to assess the degree of s -orbital parentage in the title molecules and to provide support for the experimentally observed EPR parameters. Calculations at the exact two-component (X2C) Hamiltonian in the diagonal local approximation to the unitary decoupling transformation^{41,42} (DLU) and the B3LYP/x2c-TZVPall- s level^{43–45} indicate that the SOMOs (Figure 5) of **1–3** contain considerable $6s$ character, similar to previously reported divalent lanthanocenes.^{14,27,29,32,46} In the report of a 3.467 GHz hyperfine coupling observed for the $[\text{Lu}(\text{OAr})_3]^-$ system mentioned above, more standard DFT methods failed to capture the hyperfine coupling constants, overshooting by an order of magnitude.¹⁴ However, the more rigorous DLU-X2C framework has recently been shown to be effective in modeling

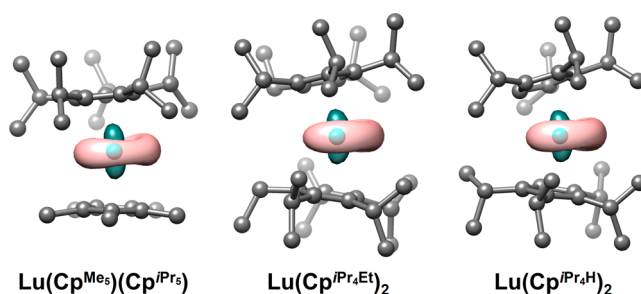


Figure 5. Singly occupied molecular orbitals (SOMOs) corresponding to complexes **1–3** at the B3LYP/x2c-TZVPall- s /scalar-relativistic DLU-X2C level are shown at an isosurface value of 0.07.

hyperfine tensors for systems with particularly large hyperfine coupling constants.^{47–51} This method was indeed found to accurately capture the experimentally measured g and hyperfine tensors for **1–3** at the $\omega\text{B97X-D}/x2c\text{-TZVPall-}s$ level^{51,52} (Tables S16–S21) as well as with other functionals (see included Supporting Information). All functionals screened strongly reflect the trend of decreasing hyperfine coupling from **1** to **2** and to **3**.

At the scalar-relativistic level of calculation, the large hyperfine coupling constants are almost entirely derived from the Fermi-contact interaction, with only vanishingly small contributions from both the paramagnetic spin–orbital interaction and the nuclear-electron spin–dipolar coupling interaction (Tables S13–S15 and S19–S21). The minor impact of spin–orbit terms is also confirmed by the results of the spin–orbit two-component calculations. This clearly confirms that the Fermi-contact term is the origin of the massive hyperfine coupling constants through pronounced $6s$ mixing; indeed, both the Fermi-contact contribution to the hyperfine coupling constant and the spin density at the ^{175}Lu nucleus decrease gradually from **1** to **2** to **3** (Figures S27 and S28). Natural population analysis (Table S22) on the SOMOs of **1–3** yields $6s$ orbital parentages of 43.3%, 42.7%, and 41.7% for **1**, **2**, and **3**, respectively, correlating (Figures S29 and S30) with $6s$ -orbital characters of 41.2%, 40.5%, and 39.2% derived from experimentally determined hyperfine coupling constants.

Note that an s -orbital character of 50% represents the maximum theoretical value for any system where the orbital that incurs an s -orbital admixture, in this case the $5d_z^2$ orbital, lies energetically below the corresponding admixing s -orbital prior to mixing considerations, in this case the $6s$ orbital. This energetic ordering of the $5d_z^2$ orbital below the $6s$ orbital prior to mixing considerations is validated by the greater $5d_z^2$ character than $6s$ character for **1–3** via natural population analysis (Table S23). If $5d_z^2$ is the majority contributor to the lower-energy $5d_z^2 - 6s$ hybrid orbital, then naturally the $5d_z^2$ orbital must be energetically lower than the $6s$ orbital prior to orbital mixing considerations. Thus, since an s -orbital character of 50% represents the maximum theoretical value for systems such as these, the observed 41.2% s -orbital character for **1** corresponds to 82.4% of the maximum possible $6s$ orbital character for a Lu^{2+} complex.

CONCLUSIONS

The foregoing results demonstrate that the introduction of axial crystal fields—in the form of bulky cyclopentadienyl ligands—in Lu^{2+} complexes gives rise to hyperfine coupling of unprecedented magnitude among lanthanide complexes.

Further, EPR and computational analyses confirm that this large hyperfine coupling arises owing to the presence of a $5d_{z^2} - 6s$ SOMO marked by up to 41.2% $6s$ character, representing the highest degree of s -orbital character yet reported for the ground state of an open-shell molecule, as well as near-record magnitudes of hyperfine coupling constants greater than 4 GHz. Across the three Lu^{2+} metallocene complexes, varying degrees of axiality act to further fine-tune the core magnetic properties and establish a clear trend among the geometric structure, crystal field axiality, and s -orbital parentage of the singly occupied molecular orbitals. By combining isotopic substitution to ^{176}Lu —where the larger $I = 7$ nuclear spin also increases clock transition energies—with a further strengthening of the hyperfine coupling via crystal field considerations, it may be possible to realize Lu^{2+} clock qubits operative at even higher frequencies.

More broadly, these results outline a synthetic approach toward molecules with true ^2S ground states, which may find use in areas of quantum information science within and beyond clock qubits, such as the design of optically or electrically addressable nuclear spin qubits. Toward this end, work is underway to further adjust the chemical periphery of bulky cyclopentadienyl ligands to enforce more linear geometries as well as to extend this approach to other axial ligand families and to other metal ions, especially metal ions inherently capable of even larger hyperfine interactions.

■ ASSOCIATED CONTENT

SI Supporting Information

The Supporting Information is available free of charge at <https://pubs.acs.org/doi/10.1021/jacs.5c01947>.

Experimental section, synthetic procedures, IR, UV–vis–NIR, EPR spectroscopy data, X-ray crystallography data, and computational data (PDF)

Computational data full spreadsheets and optimized structures (ZIP)

Accession Codes

Deposition Numbers 2378861–2378863 and 2378890 contain the supplementary crystallographic data for this paper. These data can be obtained free of charge via the joint Cambridge Crystallographic Data Centre (CCDC) and Fachinformationszentrum Karlsruhe [Access Structures service](#).

■ AUTHOR INFORMATION

Corresponding Authors

K. Randall McClain — U.S. Navy, Naval Air Warfare Center, Weapons Division, Research Department, Chemistry Division, China Lake, California 93555, United States; orcid.org/0000-0001-8072-8402; Email: kenneth.r.mcclain7.civ@us.navy.mil

Stephen Hill — National High Magnetic Field Laboratory, Florida State University, Tallahassee, Florida 32310, United States; Department of Physics and Department of Chemistry and Biochemistry, Florida State University, Tallahassee, Florida 32306, United States; orcid.org/0000-0001-6742-3620; Email: shill@magnet.fsu.edu

Jeffrey R. Long — Department of Chemistry, University of California, Berkeley, Berkeley, California 94720, United States; Department of Chemical and Biomolecular Engineering, University of California, Berkeley, Berkeley, California 94720, United States; Materials Sciences Division, Lawrence Berkeley National Laboratory, Berkeley, California

94720, United States; orcid.org/0000-0002-5324-1321; Email: jrlong@berkeley.edu

Authors

Danh X. Ngo — Department of Chemistry, University of California, Berkeley, Berkeley, California 94720, United States

Jakub Hrubý — National High Magnetic Field Laboratory, Florida State University, Tallahassee, Florida 32310, United States; orcid.org/0000-0003-4947-3688

Yannick J. Franzke — Fachbereich Chemie, Philipps-Universität Marburg, 35032 Marburg, Germany; Present Address: Institute of Nanotechnology, Karlsruhe Institute of Technology (KIT), Kaiserstr. 12, 76131 Karlsruhe, Germany; orcid.org/0000-0002-8344-113X

Krishnendu Kundu — National High Magnetic Field Laboratory, Florida State University, Tallahassee, Florida 32310, United States; Present Address: Homi Bhabha Centre for Science Education, Tata Institute of Fundamental Research, Mumbai, Maharashtra 400088, India

Hyunchul Kwon — Department of Chemistry, University of California, Berkeley, Berkeley, California 94720, United States

Colin A. Gould — Department of Chemistry, University of California, Berkeley, Berkeley, California 94720, United States; orcid.org/0000-0001-9539-1582

Benjamin G. Harvey — U.S. Navy, Naval Air Warfare Center, Weapons Division, Research Department, Chemistry Division, China Lake, California 93555, United States; orcid.org/0000-0003-2091-3539

Complete contact information is available at:

<https://pubs.acs.org/doi/10.1021/jacs.5c01947>

Author Contributions

[○]D.X.N. and K.R.M. contributed equally.

Notes

The authors declare no competing financial interest.

■ ACKNOWLEDGMENTS

This research was funded by the U.S. Department of Energy, Office of Science, Office of Basic Energy Sciences, Division of Chemical Sciences, Geosciences, and Biosciences at LBNL under contract no. DE-AC02-05CH11231. The contributions of K.R.M. and B.G.H. were supported by the Naval Air Warfare Center, Weapons Division ILIR program. Work performed at the National High Magnetic Field Laboratory is supported by the US National Science Foundation (DMR-2128556) and the State of Florida. The authors thank Simon J. Teat for helpful discussions concerning X-ray crystallography.

■ REFERENCES

- (1) Parker, R. A.; Arjona Martínez, J.; Chen, K. C.; Stramma, A. M.; Harris, I. B.; Michaels, C. P.; Trusheim, M. E.; Hayhurst Appel, M.; Purser, C. M.; Roth, W. G.; Englund, D.; Atatüre, M. A Diamond Nanophotonic Interface with an Optically Accessible Deterministic Electronuclear Spin Register. *Nat. Photonics* **2024**, *18* (2), 156–161.
- (2) Wolfowicz, G.; Tyryshkin, A. M.; George, R. E.; Riemann, H.; Abrosimov, N. V.; Becker, P.; Pohl, H.-J.; Thewalt, M. L. W.; Lyon, S. A.; Morton, J. J. L. Atomic Clock Transitions in Silicon-Based Spin Qubits. *Nat. Nanotechnol.* **2013**, *8* (8), 561–564.

- (3) Morello, A.; Pla, J. J.; Bertet, P.; Jamieson, D. N. Donor Spins in Silicon for Quantum Technologies. *Adv. Quantum Technol.* **2020**, *3* (11), 2000005.
- (4) Stark, A.; Aharon, N.; Huck, A.; El-Ella, H. A. R.; Retzker, A.; Jelezko, F.; Andersen, U. L. Clock Transition by Continuous Dynamical Decoupling of a Three-Level System. *Sci. Rep.* **2018**, *8* (1), 14807.
- (5) Miao, K. C.; Blanton, J. P.; Anderson, C. P.; Bourassa, A.; Crook, A. L.; Wolfowicz, G.; Abe, H.; Ohshima, T.; Awschalom, D. D. Universal Coherence Protection in a Solid-State Spin Qubit. *Science* **2020**, *369* (6510), 1493–1497.
- (6) Hemmer, P. Multiplicative Suppression of Decoherence. *Science* **2020**, *369* (6510), 1432–1433.
- (7) Probst, S.; Zhang, G.; Rančić, M.; Ranjan, V.; Le Dantec, M.; Zhang, Z.; Albanese, B.; Doll, A.; Liu, R. B.; Morton, J.; Chancelière, T.; Goldner, P.; Vion, D.; Esteve, D.; Bertet, P. Hyperfine Spectroscopy in a Quantum-Limited Spectrometer. *Magn. Reson.* **2020**, *1* (2), 315–330.
- (8) Onizhuk, M.; Miao, K. C.; Blanton, J. P.; Ma, H.; Anderson, C. P.; Bourassa, A.; Awschalom, D. D.; Galli, G. Probing the Coherence of Solid-State Qubits at Avoided Crossings. *PRX Quantum* **2021**, *2* (1), 010311.
- (9) Davidsson, J.; Onizhuk, M.; Vorwerk, C.; Galli, G. Discovery of Atomic Clock-like Spin Defects in Simple Oxides from First Principles. *Nat. Commun.* **2024**, *15*, 4812.
- (10) Thiele, S.; Balestro, F.; Ballou, R.; Klyatskaya, S.; Ruben, M.; Wernsdorfer, W. Electrically Driven Nuclear Spin Resonance in Single-Molecule Magnets. *Science* **2014**, *344* (6188), 1135–1138.
- (11) Lavroff, R. H.; Pennington, D. L.; Hua, A. S.; Li, B. Y.; Williams, J. A.; Alexandrova, A. N. Recent Innovations in Solid-State and Molecular Qubits for Quantum Information Applications. *J. Phys. Chem. Lett.* **2021**, *12* (44), 10742–10745.
- (12) Gaita-Ariño, A.; Luis, F.; Hill, S.; Coronado, E. Molecular Spins for Quantum Computation. *Nat. Chem.* **2019**, *11* (4), 301–309.
- (13) Shiddiq, M.; Komijani, D.; Duan, Y.; Gaita-Ariño, A.; Coronado, E.; Hill, S. Enhancing Coherence in Molecular Spin Qubits via Atomic Clock Transitions. *Nature* **2016**, *531* (7594), 348–351.
- (14) Kundu, K.; White, J. R. K.; Moehring, S. A.; Yu, J. M.; Ziller, J. W.; Furche, F.; Evans, W. J.; Hill, S. A 9.2-GHz Clock Transition in a Lu(II) Molecular Spin Qubit Arising from a 3,467-MHz Hyperfine Interaction. *Nat. Chem.* **2022**, *14* (4), 392–397.
- (15) Bayliss, S. L.; Deb, P.; Laorenza, D. W.; Onizhuk, M.; Galli, G.; Freedman, D. E.; Awschalom, D. D. Enhancing Spin Coherence in Optically Addressable Molecular Qubits through Host-Matrix Control. *Phys. Rev. X* **2022**, *12* (3), 031028.
- (16) Smith, P. W.; Hrubý, J.; Evans, W. J.; Hill, S.; Minasian, S. G. Identification of an X-Band Clock Transition in Cp_3Pr^- Enabled by a $4f^2d^1$ Configuration. *J. Am. Chem. Soc.* **2024**, *146* (9), 5781–5785.
- (17) Stewart, R.; Canaj, A. B.; Liu, S.; Regincós Martí, E.; Celmina, A.; Nichol, G.; Cheng, H.-P.; Murrie, M.; Hill, S. Engineering Clock Transitions in Molecular Lanthanide Complexes. *J. Am. Chem. Soc.* **2024**, *146* (16), 11083–11094.
- (18) Collett, C. A.; Santini, P.; Carretta, S.; Friedman, J. R. Constructing Clock-Transition-Based Two-Qubit Gates from Dimers of Molecular Nanomagnets. *Phys. Rev. Res.* **2020**, *2* (3), 032037.
- (19) Kundu, K.; Chen, J.; Hoffman, S.; Marbey, J.; Komijani, D.; Duan, Y.; Gaita-Ariño, A.; Stanton, J.; Zhang, X.; Cheng, H.-P.; Hill, S. Electron-Nuclear Decoupling at a Spin Clock Transition. *Commun. Phys.* **2023**, *6*, 38.
- (20) Giménez-Santamarina, S. M.; Cardona-Serra, S.; Juan, J. M. C.; Gaita-Ariño, A.; Coronado, E. Exploiting Clock Transitions for the Chemical Design of Resilient Molecular Spin Qubits. *Chem. Sci.* **2020**, *11*, 10718–10728.
- (21) Abragam, A.; Horowitz, J.; Pryce, M. H. L.; Morton, K. W. On the Hyperfine Structure of Paramagnetic Resonance: The s-Electron Effect. *Proc. R. Soc. London Ser. Math. Phys. Sci.* **1955**, *230* (1181), 169–187.
- (22) McGarvey, B. R. The Isotropic Hyperfine Interaction. *J. Phys. Chem.* **1967**, *71* (1), 51–66.
- (23) Munzarová, M. L.; Kubáček, P.; Kaupp, M. Mechanisms of EPR Hyperfine Coupling in Transition Metal Complexes. *J. Am. Chem. Soc.* **2000**, *122* (48), 11900–11913.
- (24) Bruzewicz, C. D.; Chiaverini, J.; McConnell, R.; Sage, J. M. Trapped-Ion Quantum Computing: Progress and Challenges. *Appl. Phys. Rev.* **2019**, *6* (2), 021314.
- (25) Langer, C.; Ozeri, R.; Jost, J. D.; Chiaverini, J.; DeMarco, B.; Ben-Kish, A.; Blakestad, R. B.; Britton, J.; Hume, D. B.; Itano, W. M.; Leibfried, D.; Reichle, R.; Rosenband, T.; Schaetz, T.; Schmidt, P. O.; Wineland, D. J. Long-Lived Qubit Memory Using Atomic Ions. *Phys. Rev. Lett.* **2005**, *95* (6), 060502.
- (26) Olmschenk, S.; Younge, K. C.; Moehring, D. L.; Matsukevich, D.; Maunz, P.; Monroe, C. Manipulation and Detection of a Trapped Yb^+ Ion Hyperfine Qubit. *Phys. Rev. A* **2007**, *76* (5), 052314.
- (27) MacDonald, M. R.; Bates, J. E.; Ziller, J. W.; Furche, F.; Evans, W. J. Completing the Series of + 2 Ions for the Lanthanide Elements: Synthesis of Molecular Complexes of Pr^{2+} , Gd^{2+} , Tb^{2+} , and Lu^{2+} . *J. Am. Chem. Soc.* **2013**, *135* (26), 9857–9868.
- (28) Martin, W. C.; Zalubas, R.; Hagan, L. *Atomic Energy Levels - the Rare Earth Elements. (the Spectra of Lanthanum, Cerium, Praseodymium, Neodymium, Promethium, Samarium, Europium, Gadolinium, Terbium, Dysprosium, Holmium, Erbium, Thulium, Ytterbium, and Lutetium).* [66 Atoms and Ions]; PB-282067; NSRDS-NBS-60; Manchester Coll. of Science and Technology (UK). Department of Chemistry, 1978. <https://www.osti.gov/biblio/6507735>. accessed 2025 January 26.
- (29) McClain, K. R.; Gould, C. A.; Marchiori, D. A.; Kwon, H.; Nguyen, T. T.; Rosenkoetter, K. E.; Kuzmina, D.; Tuna, F.; Britt, R. D.; Long, J. R.; Harvey, B. G. Divalent Lanthanide Metallocene Complexes with a Linear Coordination Geometry and Pronounced 6s–5d Orbital Mixing. *J. Am. Chem. Soc.* **2022**, *144* (48), 22193–22201.
- (30) Protchenko, A. V.; Dange, D.; Harmer, J. R.; Tang, C. Y.; Schwarz, A. D.; Kelly, M. J.; Phillips, N.; Tirfoin, R.; Birj Kumar, K. H.; Jones, C.; Kaltsoyannis, N.; Mountford, P.; Aldridge, S. Stable GaX_2 , InX_2 and TiX_2 Radicals. *Nat. Chem.* **2014**, *6* (4), 315–319.
- (31) Uson, R.; Fornies, J.; Tomas, M.; Garde, R.; Alonso, P. J. Synthesis and Structure of $(\text{NBu}_4)_2[\text{Ti}\{\text{Pt}(\text{C}_6\text{F}_5)_4\}_2]$, the First Paramagnetic Compound Containing Thallium(II). *J. Am. Chem. Soc.* **1995**, *117* (6), 1837–1838.
- (32) Gould, C. A.; McClain, K. R.; Yu, J. M.; Groshens, T. J.; Furche, F.; Harvey, B. G.; Long, J. R. Synthesis and Magnetism of Neutral, Linear Metallocene Complexes of Terbium(II) and Dysprosium(II). *J. Am. Chem. Soc.* **2019**, *141* (33), 12967–12973.
- (33) Gould, C. A.; McClain, K. R.; Reta, D.; Kragoskow, J. G. C.; Marchiori, D. A.; Lachman, E.; Choi, E.-S.; Analytis, J. G.; Britt, R. D.; Chilton, N. F.; Harvey, B. G.; Long, J. R. Ultrahard Magnetism from Mixed-Valence Dilanthanide Complexes with Metal-Metal Bonding. *Science* **2022**, *375* (6577), 198–202.
- (34) Goodwin, C. A. P.; Reta, D.; Ortu, F.; Chilton, N. F.; Mills, D. P. Synthesis and Electronic Structures of Heavy Lanthanide Metallocenium Cations. *J. Am. Chem. Soc.* **2017**, *139* (51), 18714–18724.
- (35) Liu, J.; Reta, D.; Cleghorn, J. A.; Yeoh, Y. X.; Ortu, F.; Goodwin, C. A. P.; Chilton, N. F.; Mills, D. P. Light Lanthanide Metallocenium Cations Exhibiting Weak Equatorial Anion Interactions. *Chem. – Eur. J.* **2019**, *25* (32), 7749–7758.
- (36) Weil, J. A.; Bolton, J. R. *Electron Paramagnetic Resonance: Elementary Theory and Practical Applications*; John Wiley & Sons, 2007.
- (37) Stoll, S.; Schweiger, A. EasySpin, a Comprehensive Software Package for Spectral Simulation and Analysis in EPR. *J. Magn. Reson.* **2006**, *178* (1), 42–55.
- (38) Ramanathan, A.; Walter, E. D.; Mourigal, M.; La Pierre, H. S. Increased Crystal Field Drives Intermediate Coupling and Minimizes Decoherence in Tetravalent Praseodymium Qubits. *J. Am. Chem. Soc.* **2023**, *145* (32), 17603–17612.

- (39) Schwamm, R. J.; Harmer, J. R.; Lein, M.; Fitchett, C. M.; Granville, S.; Coles, M. P. Isolation and Characterization of a Bismuth(II) Radical. *Angew. Chem., Int. Ed.* **2015**, *54* (36), 10630–10633.
- (40) Morton, J. R.; Preston, K. F. Atomic Parameters for Paramagnetic Resonance Data. *J. Magn. Reson.* **1978**, *30* (3), 577–582.
- (41) Peng, D.; Mikkelsen, N.; Weigend, F.; Reiher, M. An Efficient Implementation of Two-Component Relativistic Exact-Decoupling Methods for Large Molecules. *J. Chem. Phys.* **2013**, *138* (18), 184105.
- (42) Franzke, Y. J.; Mikkelsen, N.; Weigend, F. Efficient Implementation of One- and Two-Component Analytical Energy Gradients in Exact Two-Component Theory. *J. Chem. Phys.* **2018**, *148* (10), 104110.
- (43) Becke, A. D. Density-Functional Exchange-Energy Approximation with Correct Asymptotic Behavior. *Phys. Rev. A* **1988**, *38* (6), 3098–3100.
- (44) Lee, C.; Yang, W.; Parr, R. G. Development of the Colle-Salvetti Correlation-Energy Formula into a Functional of the Electron Density. *Phys. Rev. B* **1988**, *37* (2), 785–789.
- (45) Franzke, Y. J.; Treß, R.; Pazdera, T. M.; Weigend, F. Error-Consistent Segmented Contracted All-Electron Relativistic Basis Sets of Double- and Triple-Zeta Quality for NMR Shielding Constants. *Phys. Chem. Chem. Phys.* **2019**, *21* (30), 16658–16664.
- (46) Jin, P.-B.; Luo, Q.-C.; Gransbury, G. K.; Vitorica-Yrezabal, I. J.; Hajdu, T.; Strashnov, I.; McInnes, E. J. L.; Winpenny, R. E. P.; Chilton, N. F.; Mills, D. P.; Zheng, Y.-Z. Thermally Stable Terbium(II) and Dysprosium(II) Bis-Amidinate Complexes. *J. Am. Chem. Soc.* **2023**, *145* (51), 27993–28009.
- (47) Franzke, Y. J.; Yu, J. M. Hyperfine Coupling Constants in Local Exact Two-Component Theory. *J. Chem. Theory Comput.* **2022**, *18* (1), 323–343.
- (48) Franzke, Y. J.; Yu, J. M. Quasi-Relativistic Calculation of EPR g Tensors with Derivatives of the Decoupling Transformation, Gauge-Including Atomic Orbitals, and Magnetic Balance. *J. Chem. Theory Comput.* **2022**, *18* (4), 2246–2266.
- (49) Holzer, C.; Franzke, Y. J.; Pausch, A. Current Density Functional Framework for Spin-Orbit Coupling. *J. Chem. Phys.* **2022**, *157* (20), 204102.
- (50) Gillhuber, S.; Franzke, Y. J.; Weigend, F. Paramagnetic NMR Shielding Tensors and Ring Currents: Efficient Implementation and Application to Heavy Element Compounds. *J. Phys. Chem. A* **2021**, *125* (44), 9707–9723.
- (51) Bruder, F.; Franzke, Y. J.; Weigend, F. Paramagnetic NMR Shielding Tensors Based on Scalar Exact Two-Component and Spin-Orbit Perturbation Theory. *J. Phys. Chem. A* **2022**, *126* (30), 5050–5069.
- (52) Chai, J.-D.; Head-Gordon, M. Long-Range Corrected Hybrid Density Functionals with Damped Atom-Atom Dispersion Corrections. *Phys. Chem. Chem. Phys.* **2008**, *10* (44), 6615–6620.



CAS BIOFINDER DISCOVERY PLATFORM™

PRECISION DATA FOR FASTER DRUG DISCOVERY

CAS BioFinder helps you identify
targets, biomarkers, and pathways

Unlock insights

CAS
A division of the
American Chemical Society